**Article:**

Karageorghis, A. and Lesnic, D. orcid.org/0000-0003-3025-2770 (2024) The method of fundamental solutions for solving scattering problems from infinite elastic thin plates. Computers & Structures, 301. 107419. ISSN 0045-7949

https://doi.org/10.1016/j.compstruc.2024.107419

# THE METHOD OF FUNDAMENTAL SOLUTIONS FOR SOLVING SCATTERING PROBLEMS FROM INFINITE ELASTIC THIN PLATES

ANDREAS KARAGEORGHIS AND DANIEL LESNIC

Abstract. We investigate different variants of the method of fundamental solutions for solving scattering problems from infinite elastic thin plates. These provide novelty and desirable ease of implementation as direct accurate and fast solvers to be used iteratively in solving the corresponding inverse problems. Various direct problems associated with physical states of clamped, simply supported, roller–supported and free plates can be solved efficiently using the proposed meshless method. In particular, the numerical implementation performed for clamped plates leads to results showing very good agreement with the analytical solution, where available, and with previously obtained boundary integral method solutions. As for the inverse obstacle identification, the study further develops a constrained nonlinear regularization method for identifying a cavity concealed in an infinite elastic thin plate that has important benefits to the structural monitoring of aircraft components using non–destructing material testing.

## 1. Introduction

In the context of the Helmholtz equation and Maxwell system being the two main models of acoustic and electromagnetic scattering from obstacles, respectively, [9], recently, a few studies on the scattering of biharmonic waves in thin plate elasticity have emerged [10, 21, 22, 24]. These resulted from two active engineering areas. One is seismic cloaking aimed at protecting an infrastructure from earthquakes [26], and the other is the use of platonic crystals designed to harness or guide destructive wave energy for constructive purposes [10, 11].

Prior to this study, boundary integral methods (BIMs) [3, 10, 24] have been developed for solving the direct scattering of flexural waves on thin plates such as those governed by equations (2.1)–(2.3) below when the cavity $D$ is known. Interior associated vibration problems when the governing equation (2.1) holds inside the bounded domain $D$ have also been considered using BIMs in [20,23,27] and, in [13,14], using the boundary particle method. In Section 3 we propose, apparently for the first time, several meshless techniques based on the method of fundamental solutions (MFS) [12]. This is a versatile alternative to BIMs for solving such problems because it does not require meshing. Moreover, in Section 5 we investigate numerically the corresponding inverse scattering problem, which requires identifying impenetrable obstacles from multistatic near–field data.

*Date*: May 21, 2024.
2000 *Mathematics Subject Classification.* Primary 65N35; Secondary 65N21, 65N38.
*Key words and phrases.* Wave scattering, infinite elastic thin plates, method of fundamental solutions.

## 2. Mathematical formulation

We consider the scattering by an impenetrable planar bounded obstacle $D \subset \mathbb{R}^2$ with sufficiently smooth boundary, e.g. of class $C^3$, in an infinite elastic Kirchhoff–Love thin (thickness $h \ll 2\pi/\kappa$) plate connected medium $\Omega = \mathbb{R}^2 \backslash \overline{D}$ given by (in the frequency domain), see [4],

$$\Delta^2 v^{\mathrm{s}} - \kappa^4 v^{\mathrm{s}} \;=\; 0 \quad \text{in} \quad \Omega, \tag{2.1}$$

subject to the radiation infinity condition

$$\lim_{r\to\infty} \int_{\partial B_r(\mathbf{0})} \left| \frac{\partial v^{\mathrm{s}}}{\partial r} - \mathrm{i}\kappa v^{\mathrm{s}} \right|^2 ds = 0 \tag{2.2}$$

and the boundary conditions

$$\mathcal{B}_1(v^{\mathrm{s}} + u^{\mathrm{inc}}) = \mathcal{B}_2(v^{\mathrm{s}} + u^{\mathrm{inc}}) = 0 \quad \text{on} \quad \partial D = \partial\Omega, \tag{2.3}$$

where $v^{\mathrm{s}}$ is the scattered field, $\kappa > 0$ is the wave number satisfying $\kappa^2 = \omega\sqrt{\varrho h/\mathcal{D}}$, where $\omega$ is the angular frequency, $\varrho$ is the mass density and $\mathcal{D}$ is the flexural rigidity of the plate. Also, $B_r(\mathbf{0}) = \{\boldsymbol{x} \in \mathbb{R}^2 |\, |\boldsymbol{x}| < r\}$ is the disk centred at the origin of radius $r > 0$, $u^{\mathrm{inc}}$ is an incident field satisfying $\Delta^2 u^{\mathrm{inc}} - \kappa^4 u^{\mathrm{inc}} = 0$ in $\mathbb{R}^2$ (for example, a plane wave $u^{\mathrm{inc}}(x_1, x_2) = \mathrm{e}^{\mathrm{i}\kappa x_1}$), and $\mathcal{B}_1$ and $\mathcal{B}_2$ are boundary operators giving the boundary conditions on $\partial D$, for example:

(i) $\mathcal{B}_1 = I,\ \mathcal{B}_2 = \partial/\partial n$ (clamped plate)
(ii) $\mathcal{B}_1 = I,\ \mathcal{B}_2 = \mathcal{M}$ (simply supported plate)
(iii) $\mathcal{B}_1 = \partial/\partial n,\ \mathcal{B}_2 = \mathcal{N}$ (roller–supported plate)
(iv) $\mathcal{B}_1 = \mathcal{M},\ \mathcal{B}_2 = \mathcal{N}$ (free plate),

where $\boldsymbol{n} = (n_1, n_2)$ is the inward unit normal to $D$, $I$ is the identity trace operator, and $\mathcal{M}$ and $\mathcal{N}$ are the normalised bending moment and transverse force given by, see [15],

$$\mathcal{M}u := \nu\Delta u + (1-\nu)\mathcal{M}_0 u, \quad \mathcal{N}u := -\frac{\partial(\Delta u)}{\partial n} - \frac{\partial(\mathcal{N}_0 u)}{\partial t}, \tag{2.4}$$

$\boldsymbol{t} = (-n_2, n_1)$ is the tangent unit vector to $\partial D$, $\nu \in [0, 0.5)$ is the Poisson's ratio and

$$\mathcal{M}_0 u = \frac{\partial^2 u}{\partial x_1^2} n_1^2 + 2\frac{\partial^2 u}{\partial x_1 \partial x_2} n_1 n_2 + \frac{\partial^2 u}{\partial x_2^2} n_2^2, \quad \mathcal{N}_0 u = \frac{\partial^2 u}{\partial x_1 \partial x_2}\left(n_1^2 - n_2^2\right) - \left(\frac{\partial^2 u}{\partial x_1^2} - \frac{\partial^2 u}{\partial x_2^2}\right) n_1 n_2.$$

The clamped and free plate boundary conditions (i) and (iv) correspond to the Dirichlet and Neumann boundary conditions associated with the fourth–order partial differential equation (2.1) and physically they specify the plane displacement and the angle of rotation of the plate, and the bending moment and the shear force, respectively, [5]. The unique solvability for the scattered field $v^{\mathrm{s}} \in H^2_{\mathrm{loc}}(\Omega)$ satisfying the direct problem (2.1)–(2.3) in cases (i), (ii) or (iii) for any $\kappa > 0$ holds [4]. In the case of free plates (iv) (modelling a hole $D$ within the infinite plate) the unique solvability holds for any $\kappa > 0$ except for a countable set of wavenumbers $(\kappa_{\mathsf{n}})_{\mathsf{n}\in\mathbb{N}}$ satisfying $\lim_{\mathsf{n}\to\infty} \kappa_{\mathsf{n}} = \infty$. Note that in [10], the radiation condition (2.2) is replaced by the conditions

$$\lim_{r\to\infty} \sqrt{r}\left(\frac{\partial v^{\mathrm{s}}}{\partial r} - \mathrm{i}\kappa v^{\mathrm{s}}\right) = 0 = \lim_{r\to\infty} \sqrt{r}\left(\frac{\partial(\Delta v^{\mathrm{s}})}{\partial r} - \mathrm{i}\kappa \Delta v^{\mathrm{s}}\right). \tag{2.5}$$

Also, the radiation condition (2.2) is the same as the Sommerfeld radiation condition used for the Helmholtz equation in acoustic scattering, see [9,15]. As remarked in [5], the reason why only one radiation condition (2.2) is needed instead of a pair is that $v^{\mathrm{s}}$ can be written as the superposition of a propagative part $v^{\mathrm{pr}} = -\frac{1}{2\kappa^2}\left(\Delta v^{\mathrm{s}} - \kappa^2 v^{\mathrm{s}}\right)$ satisfying the Helmholtz equation in $\Omega$ and an evanescent part $v^{\mathrm{ev}} = \frac{1}{2\kappa^2}\left(\Delta v^{\mathrm{s}} + \kappa^2 v^{\mathrm{s}}\right)$ satisfying the modified Helmholtz equation in $\Omega$, which does not contribute to the far field since it is exponentially decaying. Furthermore, in addition to $v^{\mathrm{s}} = v^{\mathrm{pr}} + v^{\mathrm{ev}}$ we also have that $\Delta v^{\mathrm{s}} = \kappa^2\left(v^{\mathrm{ev}} - v^{\mathrm{pr}}\right)$.

## 3. The method of fundamental solutions (MFS)

We have implemented the following four MFS approaches for the solution of boundary value problem (2.1)–(2.3):

3.1. **First approach.** We approximate the solution of (2.1)–(2.3) by a linear combination of non–singular fundamental solutions [29]

$$v_N^{\mathrm{s}}(\boldsymbol{x}) = \sum_{j=1}^{2N} c_j\, G(\boldsymbol{x}, \boldsymbol{\xi}_j), \quad \boldsymbol{x} \in \overline{\Omega} = \Omega \cup \partial\Omega, \tag{3.1}$$

where $\left(\boldsymbol{\xi}_j\right)_{j=\overline{1,2N}}$ are source points located inside $D$ and $\left(c_j\right)_{j=\overline{1,2N}}$ are unknown complex coefficients to be determined by imposing the boundary conditions (2.3). In (3.1), $G$ is the fundamental solution of the operator in equation (2.1), which in two dimensions is given by, see [21],

$$G(\boldsymbol{x}, \boldsymbol{\xi}) = \frac{\mathrm{i}}{8\kappa^2}\left(H_0^{(1)}(\kappa|\boldsymbol{x}-\boldsymbol{\xi}|) - H_0^{(1)}(\mathrm{i}\kappa|\boldsymbol{x}-\boldsymbol{\xi}|)\right), \tag{3.2}$$

where $H_0^{(1)}$ is the Hankel function of the first kind of order zero. Note that approximation (3.1) automatically satisfies the governing equation (2.1) in $\Omega$ and the infinity condition (2.2), see [5].

Assuming that $D$ is a smooth, star–like domain with respect to the origin, in polar coordinates its boundary $\partial D$ can be parameterized as

$$x_1 = r(\vartheta)\,\cos\vartheta, \qquad x_2 = r(\vartheta)\,\sin\vartheta, \qquad \vartheta \in [0, 2\pi), \tag{3.3}$$

where $r$ is a smooth $2\pi-$periodic function. We place $M$ collocation points on $\partial D$ as follows:

$$\boldsymbol{x}_m = r(\tilde{\vartheta}_m)\left(\cos\tilde{\vartheta}_m, \sin\tilde{\vartheta}_m\right), \quad \tilde{\vartheta}_m = 2\pi(m-1)/M,\ m = \overline{1, M}. \tag{3.4}$$

We also place $N$ sources on a pseudo–boundary $\partial D'$ given by

$$\boldsymbol{\xi}_\ell = \eta_1\, r(\vartheta_\ell)\ (\cos\vartheta_\ell, \sin\vartheta_\ell), \quad \ell = \overline{1, N}, \tag{3.5}$$

and another $N$ sources on a pseudo–boundary $\partial D''$ given by

$$\boldsymbol{\xi}_{N+\ell} = \eta_2\, r(\vartheta_\ell)\ (\cos\vartheta_\ell, \sin\vartheta_\ell), \quad \ell = \overline{1, N}, \tag{3.6}$$

where $\vartheta_\ell = 2\pi(\ell-1)/N$ and the contraction parameters $\eta_1, \eta_2 \in (0, 1)$ and $\eta_1 \neq \eta_2$.

The imposition of the two boundary conditions in each of the cases (i)–(iv) yields a $2M \times 2N$ linear system of the form

$$\left[\frac{B_1}{B_2}\right] \boldsymbol{c} = \left[\frac{b_1}{b_2}\right], \tag{3.7}$$

where the matrices $B_1, B_2 \in \mathbb{R}^{M\times 2N}$ are defined by

$$B_1 = \mathcal{B}_1 G(\boldsymbol{x}_i, \boldsymbol{\xi}_j), \quad B_2 = \mathcal{B}_2 G(\boldsymbol{x}_i, \boldsymbol{\xi}_j), \quad i = \overline{1,M},\ j = \overline{1,2N},$$

and the vectors $b_1, b_2 \in \mathbb{R}^{M\times 1}$ are defined by

$$b_1 = -\mathcal{B}_1 u^{\text{inc}}(\boldsymbol{x}_i), \quad b_2 = -\mathcal{B}_2 u^{\text{inc}}(\boldsymbol{x}_i), \quad i = \overline{1,M}. \tag{3.8}$$

Having determined the vector of coefficients $\boldsymbol{c} \in \mathbb{R}^{2N\times 1}$, the approximation (3.1) may be calculated anywhere in $\overline{\Omega}$.

3.2. **Second approach.** Following the indirect boundary element formulation in [23, Section 4.1], see also [20, 27], we now approximate the solution of (2.1)–(2.3) by

$$v_N^{\text{s}}(\boldsymbol{x}) = \sum_{j=1}^{N} c_j\, G(\boldsymbol{x}, \boldsymbol{\xi}_j) + \sum_{j=1}^{N} d_j\, \frac{\partial G}{\partial n(\boldsymbol{\xi})}(\boldsymbol{x}, \boldsymbol{\xi}_j), \quad \boldsymbol{x} \in \overline{\Omega}, \tag{3.9}$$

where $\left(\boldsymbol{\xi}_j\right)_{j=\overline{1,N}}$ are source points located inside $D$ and $(c_j)_{j=\overline{1,N}}$ and $(d_j)_{j=\overline{1,N}}$ are unknown complex coefficients to be determined by imposing the boundary conditions (2.3). Note that in (3.9), $\boldsymbol{n}(\boldsymbol{\xi}) = (n_{\xi_1}, n_{\xi_2})$ is the inward unit normal to the pseudo–boundary $\partial D'$ on which the sources are placed.

Assuming that, as in Section 3.2, the boundary $\partial D$ is a smooth, star–like curve with polar coordinates described by (3.3), we again place $M$ collocation points on $\partial D$ as in (3.4). We also place $N$ sources on the pseudo–boundary $\partial D'$ given as

$$\boldsymbol{\xi}_\ell = \eta\, r(\vartheta_\ell)\, (\cos\vartheta_\ell, \sin\vartheta_\ell), \quad \ell = \overline{1,N}, \tag{3.10}$$

where the contraction parameter $\eta \in (0,1)$.

The imposition of the two boundary conditions in each of the cases (1)–(iv) yields a $2M \times 2N$ linear system of the form

$$\left[\begin{array}{c|c} B_{11} & B_{12} \\ \hline B_{21} & B_{22} \end{array}\right] \left[\frac{\boldsymbol{c}}{\boldsymbol{d}}\right] = \left[\frac{b_1}{b_2}\right], \tag{3.11}$$

where the matrices $B_{11}, B_{12}, B_{21}, B_{22} \in \mathbb{R}^{M\times N}$ are defined by

$$B_{11} = \mathcal{B}_1 G(\boldsymbol{x}_i, \boldsymbol{\xi}_j),\ B_{12} = \mathcal{B}_1 \frac{\partial G}{\partial n(\boldsymbol{\xi})}(\boldsymbol{x}_i, \boldsymbol{\xi}_j),\ B_{21} = \mathcal{B}_2 G(\boldsymbol{x}_i, \boldsymbol{\xi}_j),\ B_{22} = \mathcal{B}_2 \frac{\partial G}{\partial n(\boldsymbol{\xi})}(\boldsymbol{x}_i, \boldsymbol{\xi}_j),$$

for $i = \overline{1,M}$, $j = \overline{1,N}$, and the vectors $b_1, b_2 \in \mathbb{R}^{M\times 1}$ are defined by (3.8). Having determined the vectors of coefficients $\boldsymbol{c}, \boldsymbol{d} \in \mathbb{R}^{N\times 1}$, the approximation (3.9) may be calculated anywhere in $\overline{\Omega}$.

3.3. **Third approach.** Following the indirect boundary element formulation (3.20) in [10], we now approximate the solution of (2.1)–(2.3) by

$$v_N^{\mathrm{s}}(\boldsymbol{x}) = \sum_{k=1}^{N} c_j \, G_{\mathrm{M}}(\boldsymbol{x}, \boldsymbol{\xi}_j) + \sum_{k=1}^{N} d_j \, \frac{\partial G_{\mathrm{H}}}{\partial n(\boldsymbol{\xi})}(\boldsymbol{x}, \boldsymbol{\xi}_j), \quad \boldsymbol{x} \in \overline{\Omega}, \tag{3.12}$$

where $\left(\boldsymbol{\xi}_j\right)_{j=\overline{1,N}}$ are source points located inside $D$ and $(c_j)_{j=\overline{1,N}}$ and $(d_j)_{j=\overline{1,N}}$ are unknown complex coefficients to be determined by imposing the boundary conditions (2.3). In (3.12), $G_{\mathrm{M}}$ is the two–dimensional fundamental solution of the modified Helmholtz operator defined by

$$G_{\mathrm{M}}(\boldsymbol{x}, \boldsymbol{\xi}) = \frac{\mathrm{i}}{4} H_0^{(1)}(\mathrm{i}\kappa|\boldsymbol{x} - \boldsymbol{\xi}|), \tag{3.13}$$

while $G_{\mathrm{H}}$ is the two–dimensional fundamental solution of the Helmholtz operator defined by

$$G_{\mathrm{H}}(\boldsymbol{x}, \boldsymbol{\xi}) = \frac{\mathrm{i}}{4} H_0^{(1)}(\kappa|\boldsymbol{x} - \boldsymbol{\xi}|), \tag{3.14}$$

The discretization details are identical to those in Section 3.2.

The imposition of the two boundary conditions in each of the cases (i)–(iv) yields a $2M \times 2N$ linear system of the form

$$\left[\begin{array}{c|c} C_{11} & C_{12} \\ \hline C_{21} & C_{22} \end{array}\right] \left[\begin{array}{c} \boldsymbol{c} \\ \hline \boldsymbol{d} \end{array}\right] = \left[\begin{array}{c} b_1 \\ \hline b_2 \end{array}\right], \tag{3.15}$$

where the matrices $C_{11}, C_{12}, C_{21}, C_{22} \in \mathbb{R}^{M \times N}$ are defined by

$$C_{11} = \mathcal{B}_1 G_{\mathrm{M}}(\boldsymbol{x}_i, \boldsymbol{\xi}_j),\ C_{12} = \mathcal{B}_1 \frac{\partial G_{\mathrm{H}}}{\partial n(\boldsymbol{\xi})}(\boldsymbol{x}_i, \boldsymbol{\xi}_j),\ C_{21} = \mathcal{B}_2 G_{\mathrm{M}}(\boldsymbol{x}_i, \boldsymbol{\xi}_j),\ C_{22} = \mathcal{B}_2 \frac{\partial G_{\mathrm{H}}}{\partial n(\boldsymbol{\xi})}(\boldsymbol{x}_i, \boldsymbol{\xi}_j),$$

for $i = \overline{1, M}$, $j = \overline{1, N}$, and the vectors $b_1, b_2 \in \mathbb{R}^{M \times 1}$ are defined by are defined by (3.8). Having determined the vectors of coefficients $\boldsymbol{c}, \boldsymbol{d} \in \mathbb{R}^{N \times 1}$, the approximation (3.12) may be calculated anywhere in $\overline{\Omega}$. We remark that if $G_H$ and $G_M$ are swapped in (3.12), then we expect a similar performance of the MFS in the framework of the third approach.

3.4. **Fourth approach.** Following the single–layer potential indirect boundary element formulation (5.3) in [10], we now approximate the solution of (2.1)–(2.3) by

$$v_N^{\mathrm{s}}(\boldsymbol{x}) = \sum_{j=1}^{N} c_j \, G_{\mathrm{M}}(\boldsymbol{x}, \boldsymbol{\xi}_j) + \sum_{j=1}^{N} d_j \, G_{\mathrm{H}}(\boldsymbol{x}, \boldsymbol{\xi}_j), \quad \boldsymbol{x} \in \overline{\Omega}, \tag{3.16}$$

where $\left(\boldsymbol{\xi}_j\right)_{j=\overline{1,N}}$ are source points located inside $D$ and $(c_j)_{j=\overline{1,N}}$ and $(d_j)_{j=\overline{1,N}}$ are unknown complex coefficients to be determined by imposing the boundary conditions (2.3). The discretization details are identical to those in Section 3.2, while assuming that $\kappa^2$ is not an interior Dirichlet eigenvalue of $-\Delta$ in $D'$, see [2,3].

The imposition of the two boundary conditions in each of the cases (i)–(iv) yields a $2M \times 2N$ linear system of the form

$$\left[\begin{array}{c|c} D_{11} & D_{12} \\ \hline D_{21} & D_{22} \end{array}\right] \left[\begin{array}{c} \boldsymbol{c} \\ \hline \boldsymbol{d} \end{array}\right] = \left[\begin{array}{c} b_1 \\ \hline b_2 \end{array}\right], \tag{3.17}$$

where the matrices $D_{11}, D_{12}, D_{21}, D_{22} \in \mathbb{R}^{M\times N}$ are defined by

$$D_{11} = \mathcal{B}_1 G_{\mathrm{M}}(\boldsymbol{x}_i, \boldsymbol{\xi}_j),\ D_{12} = \mathcal{B}_1 G_{\mathrm{H}}(\boldsymbol{x}_i, \boldsymbol{\xi}_j),\ D_{21} = \mathcal{B}_2 G_{\mathrm{M}}(\boldsymbol{x}_i, \boldsymbol{\xi}_j),\ D_{22} = \mathcal{B}_2 G_{\mathrm{H}}(\boldsymbol{x}_i, \boldsymbol{\xi}_j),$$

for $i = \overline{1, M}$, $j = \overline{1, N}$, and the vectors $b_1, b_2 \in \mathbb{R}^{M\times 1}$ are defined by (3.8). Having determined the vectors of coefficients $\boldsymbol{c}, \boldsymbol{d} \in \mathbb{R}^{N\times 1}$, the approximation (3.16) may be calculated anywhere in $\overline{\Omega}$.

## 4. Numerical examples for the direct problem (2.1)–(2.3)

The appropriate derivatives needed for the approaches described in Section 3 are provided in the Appendix. The choices of the contraction parameters $\eta_1$, $\eta_2 \in (0,1)$ with $\eta_1 \neq \eta_2$ in the first MFS approach and $\eta \in (0,1)$ in the other MFS approaches are based on trial and error. These parameters are chosen to be neither too small (close to 0) to avoid the clustering of the source points near the origin nor too large (close to 1) to avoid potential ill–conditioning caused by the small argument $|\boldsymbol{x} - \boldsymbol{\xi}|$ in the Hankel functions in expressions (3.2), (3.13) or (3.14), see also [19]. There is also the possibility of optimizing these contraction parameters [6] or to use the MFS locally [7, 8, 28] but, for simplicity, these are not considered herein.

In all the numerical examples investigated in this section we take $M = N$ such that the MFS systems of equations (3.7), (3.11), (3.15) or (3.17) are square. It is also possible to consider under–determined or over–determined scenarios [25], which occur when $M < N$ or $M > N$, respectively, but, for simplicity, these are not considered in the current study.

4.1. **Example 1.** For a rigid circular plate of radius $a$ centred at the origin the clamped plate boundary conditions (i) apply yielding the solution to (2.1)–(2.3) for $u^{\mathrm{inc}}(\boldsymbol{x}) = \mathrm{e}^{\mathrm{i}\kappa x_1}$, see [21],

$$v^{\mathrm{s}}(r, \vartheta) = \sum_{\mathsf{n}=0}^{\infty} \left[A_{\mathsf{n}} H_{\mathsf{n}}^{(1)}(\kappa r) + B_{\mathsf{n}} K_{\mathsf{n}}(\kappa r)\right] \cos(\mathsf{n}\vartheta), \quad r > a, \quad \vartheta \in [0, 2\pi), \tag{4.1}$$

where

$$A_{\mathsf{n}} = -\,\varepsilon_{\mathsf{n}}\,\mathrm{i}^{\mathsf{n}} \left[\frac{J_{\mathsf{n}}(\kappa a) K_{\mathsf{n}}'(\kappa a) - J_{\mathsf{n}}'(\kappa a) K_{\mathsf{n}}(\kappa a)}{H_{\mathsf{n}}^{(1)}(\kappa a) K_{\mathsf{n}}'(\kappa a) - H_{\mathsf{n}}^{(1)'}(\kappa a) K_{\mathsf{n}}(\kappa a)}\right],$$

$$B_{\mathsf{n}} = \frac{2\,\varepsilon_{\mathsf{n}}\,\mathrm{i}^{\mathsf{n}+1}}{\pi\kappa a\left[H_{\mathsf{n}}^{(1)}(\kappa a) K_{\mathsf{n}}'(\kappa a) - H_{\mathsf{n}}^{(1)'}(\kappa a) K_{\mathsf{n}}(\kappa a)\right]}, \quad \varepsilon_0 = 1,\ \varepsilon_{\mathsf{n}} = 2 \text{ for } \mathsf{n} \geq 1. \tag{132}$$

Details regarding the derivation of the quantities involved in (4.1) are provided in the Appendix. We carried out numerical experiments for different radii $a$ and $\kappa$ and $M = N$. The exact solution expansion was truncated at $\mathsf{n} = 30$. We also chose $\eta_1 = 0.55$ and $\eta_2 = 0.45$ in the first approach and $\eta = 0.5$ in the other approaches. The approximation and exact solution were calculated at $\mathrm{L} = 25$ uniformly distributed test points on a circle of radius $b = 2a$ and we recorded the maximum absolute error $E$. Some results showing the convergence of the MFS approaches are provided in Table 1. From this table it can be seen that the third and fourth MFS approaches are more accurate than the first and second MFS approaches.

TABLE 1. Example 1: The maximum absolute errors $E_k$ between the exact solution (4.1) truncated at $\mathsf{n} = 30$ and the $k$th MFS approach for $k = 1, 2, 3, 4$, calculated at $\mathrm{L} = 25$ uniformly distributed test points on a circle of radius $b = 2a$, for various numbers of degrees of freedom $M = N$ and values of $a$ and $\kappa$. Note that 8.94(-4) stands for the scientific notation 8.94e-04 or the standard form 8.94 $\times 10^{-4}$ of a decimal number, etc.

| $a$ | $\kappa$ | $M = N$ | $E_1$ | $E_2$ | $E_3$ | $E_4$ |
|---|---|---|---|---|---|---|
| 2.0 | 1.0 | 16 | 8.94(-4) | 8.31(-4) | 9.81(-4) | 1.97(-4) |
| 2.0 | 1.0 | 32 | 6.69(-8) | 3.42(-8) | 6.92(-8) | 4.88(-9) |
| 2.0 | 1.0 | 64 | 5.24(-14) | 3.79(-14) | 9.43(-16) | 4.04(-15) |
| 2.0 | 2.0 | 16 | 1.29(-2) | 1.29(-2) | 3.25(-3) | 3.57(-3) |
| 2.0 | 2.0 | 32 | 1.64(-6) | 1.07(-6) | 1.87(-7) | 1.09(-7) |
| 2.0 | 2.0 | 64 | 3.88(-13) | 2.71(-13) | 3.84(-15) | 1.51(-14) |
| 2.0 | 3.0 | 16 | 4.70(-1) | 4.81(-1) | 7.14(-2) | 6.80(-2) |
| 2.0 | 3.0 | 32 | 2.72(-5) | 2.14(-5) | 2.97(-7) | 1.89(-6) |
| 2.0 | 3.0 | 64 | 3.32(-12) | 2.42(-12) | 2.10(-14) | 6.93(-14) |
| 3.0 | 1.0 | 16 | 2.75(-3) | 2.62(-3) | 6.88(-4) | 8.21(-4) |
| 3.0 | 1.0 | 32 | 3.59(-7) | 2.09(-7) | 1.15(-7) | 2.44(-8) |
| 3.0 | 1.0 | 64 | 1.56(-13) | 9.20(-14) | 1.79(-15) | 6.98(-15) |
| 3.0 | 2.0 | 16 | 4.70(-1) | 4.81(-1) | 7.14(-2) | 6.80(-2) |
| 3.0 | 2.0 | 32 | 2.72(-5) | 2.14(-5) | 2.97(-7) | 1.89(-6) |
| 3.0 | 2.0 | 64 | 3.17(-12) | 2.21(-12) | 1.24(-14) | 5.68(-14) |
| 3.0 | 3.0 | 16 | 1.34 | 1.37 | 6.40(-1) | 6.38(-1) |
| 3.0 | 3.0 | 32 | 1.53(-3) | 1.50(-3) | 9.54(-5) | 1.02(-4) |
| 3.0 | 3.0 | 64 | 9.24(-11) | 5.70(-11) | 1.75(-13) | 6.29(-13) |

4.2. **Example 2.** We next examine the solution of problem (2.1)–(2.2) with the clamped boundary conditions exact solution

$$v^{\mathrm{s}}(\boldsymbol{x}) = H_0^{(1)}(\kappa|\boldsymbol{x} - \overline{\boldsymbol{x}}|) + H_0^{(1)}(\mathrm{i}\kappa|\boldsymbol{x} - \overline{\boldsymbol{x}}|), \quad \boldsymbol{x} \in \partial D, \tag{4.2}$$

$$\frac{\partial v^{\mathrm{s}}}{\partial n}(\boldsymbol{x}) = -\frac{\kappa\,(\boldsymbol{x} - \overline{\boldsymbol{x}}) \cdot \boldsymbol{n}}{|\boldsymbol{x} - \overline{\boldsymbol{x}}|} \left[ H_1^{(1)}(\kappa|\boldsymbol{x} - \overline{\boldsymbol{x}}|) + \mathrm{i}H_1^{(1)}(\mathrm{i}\kappa|\boldsymbol{x} - \overline{\boldsymbol{x}}|) \right], \quad \boldsymbol{x} \in \partial D, \tag{4.3}$$

where $\overline{\boldsymbol{x}}$ is the location of a point source in $D$, in place of (2.3). The problem (2.1), (2.2), (4.2) and (4.3) has the exact solution

$$v^{\mathrm{s}}(\boldsymbol{x}) = H_0^{(1)}(\kappa|\boldsymbol{x}-\overline{\boldsymbol{x}}|) + H_0^{(1)}(\mathrm{i}\kappa|\boldsymbol{x}-\overline{\boldsymbol{x}}|), \quad \boldsymbol{x} \in \Omega. \tag{4.4}$$

This benchmark problem was considered in [10] for various shapes $D$, with smooth boundaries $\partial D$ whose parametric representations are given by $\boldsymbol{x} = r(\vartheta)\,(\cos\vartheta, \sin\vartheta)\,,\ \vartheta \in [0, 2\pi)$, and:

(I) Bean shape: $r(\vartheta) = \dfrac{0.55\,(1 + 0.9\cos\vartheta + 0.1\sin(2\vartheta))}{1 + 0.75\cos\vartheta}$,

(II) Peach shape: $r(\vartheta) = 0.22\left(2 + \cos^2\vartheta\sqrt{1-\sin\vartheta}\right)$,

(III) Peanut shape: $r(\vartheta) = 0.275\sqrt{1 + 3\cos^2\vartheta}$.

The following non–smooth shapes with parametric representations given by $\gamma(\vartheta) = (\gamma_1(\vartheta), \gamma_2(\vartheta))\,,\ \vartheta \in [0, 2\pi)$, were also considered in [10]:

(IV) Drop shape: $\gamma_1(\vartheta) = 2\sin(\vartheta/2) - 1,\ \gamma_2(\vartheta) = -\sin\vartheta$,

(V) Heart shape: $\gamma_1(\vartheta) = (3/2)\sin(3\vartheta/2),\ \gamma_2(\vartheta) = \sin\vartheta$.

In the cases (IV) and (V), equations (3.4)–(3.6) are replaced by

$$\boldsymbol{x}_m = \Big(\gamma_1(\tilde{\vartheta}_m), \gamma_2(\tilde{\vartheta}_m)\Big)\,, \quad m = \overline{1, M}, \tag{4.5}$$

$$\boldsymbol{\xi}_\ell = \eta_1\,(\gamma_1(\vartheta_\ell), \gamma_2(\vartheta_\ell))\,, \quad \ell = \overline{1, N}, \tag{4.6}$$

and

$$\boldsymbol{\xi}_{N+\ell} = \eta_2\,(\gamma_1(\vartheta_\ell), \gamma_2(\vartheta_\ell))\,, \quad \ell = \overline{1, N}, \tag{4.7}$$

respectively.

In shapes (I)–(IV), the location of the point source was taken at $\overline{\boldsymbol{x}} = (0.1, 0.2)$, while in shape (V) at $\overline{\boldsymbol{x}} = (-0.5, 0.2)$. The five shapes considered, as well as the locations of the point source in each case, are depicted in Figure 1. As in [10], we took $\kappa = 2$. As in Example 1, we also chose $\eta_1 = 0.55$ and $\eta_2 = 0.45$ in the first approach and $\eta = 0.5$ in the other approaches. The approximation and exact solution were calculated at L = 25 uniformly distributed test points on a circle of radius 1 centred at the origin for shapes (I)–(III) and on a circle of radius 2 centred at the origin for shapes (IV)–(V). We recorded the maximum absolute error $E$ there and the discrete $L^2$-error norm $\mathcal{E} = ||v^{\mathrm{s}} - v^{\mathrm{s}}_N||_2/\sqrt{L}$. The results for different degrees of freedom for each approach and each shape presented in Tables 2 and 3 illustrate the convergence of the MFS approaches with respect to increasing the number of degrees of freedom. It is noteworthy that, due to their increased boundary curvature, the heart and peanut–shape geometries, require more degrees of freedom than the other shapes to achieve a comparable level of accuracy.

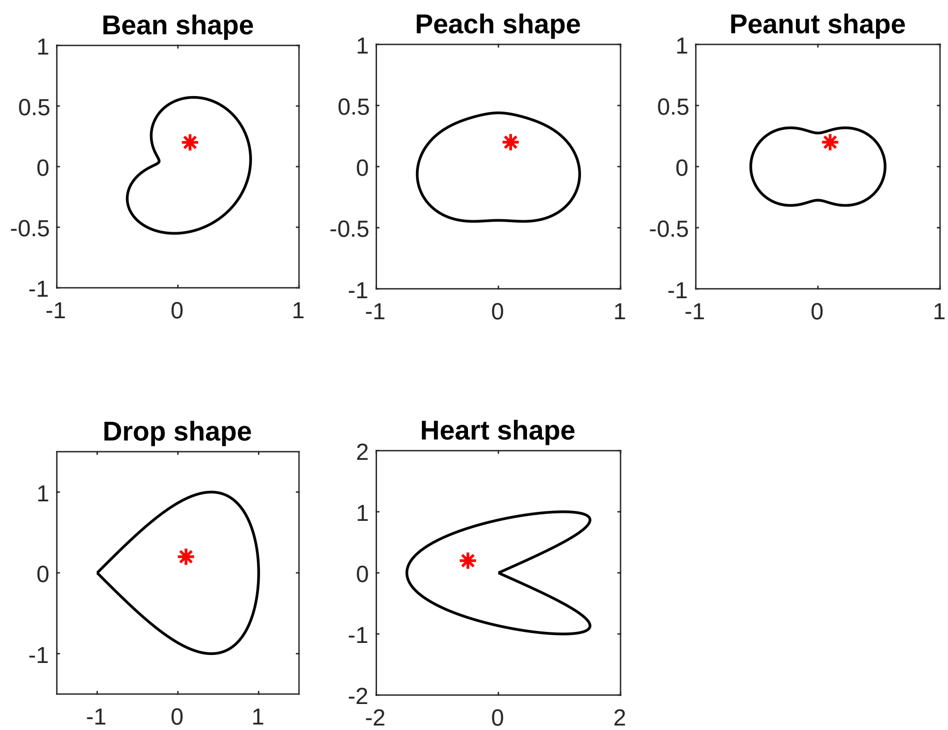


FIGURE 1. Example 2: Shapes considered. The location of the point source $\overline{\boldsymbol{x}}$ is denoted by a red asterisk $*$.

4.3. **Example 3.** As in [10], we examine the solution of problem (2.1)–(2.3) for a clamped plate when the cavity $D$ is illuminated by the plane wave with an incident angle $\pi/6$ given by

$$u^{\mathrm{inc}}(\boldsymbol{x}) = \mathrm{e}^{\mathrm{i}\kappa\boldsymbol{x}\cdot(\cos(\pi/6),\sin(\pi/6))}, \quad \boldsymbol{x} \in \mathbb{R}^2, \tag{4.8}$$

where $D$ can be any of the shapes considered in Example 2. As this problem has no analytical solution we shall use the numerical solution obtained for $M = N = 2048$ as the reference solution. For simplicity, we shall use only the third and fourth MFS approaches, and calculate the far field patterns $v^{\mathrm{s}}_{N_\infty}$ at 32 uniformly distributed observation points on the unit circle. These far field patterns are given, from [10], by

$$v^{\mathrm{s}}_{N_\infty}(\hat{\boldsymbol{x}}) = \frac{\mathrm{e}^{\mathrm{i}\pi/4}}{\sqrt{8\kappa\pi}} \sum_{j=1}^{N} d_j \, \frac{\partial\left(\mathrm{e}^{-\mathrm{i}\kappa\hat{\boldsymbol{x}}\cdot\boldsymbol{\xi}_j}\right)}{\partial n(\boldsymbol{\xi})} \quad \text{for the Third Approach} \tag{4.9}$$

and

$$v^{\mathrm{s}}_{N_\infty}(\hat{\boldsymbol{x}}) = \frac{\mathrm{e}^{\mathrm{i}\pi/4}}{\sqrt{8\kappa\pi}} \sum_{j=1}^{N} c_j \, \mathrm{e}^{-\mathrm{i}\kappa\hat{\boldsymbol{x}}\cdot\boldsymbol{\xi}_j} \quad \text{for the Fourth Approach,} \tag{4.10}$$

where $\hat{\boldsymbol{x}} = \boldsymbol{x}/r$ is the observation direction and $r = |\boldsymbol{x}|$. As in Example 2, we took $\kappa = 2$ and chose $\eta = 0.5$.

TABLE 2. Example 2: The maximum absolute error $E$ and the discrete $L^2$-error norm $\mathcal{E}$ between the exact solution (4.4) and the MFS approaches calculated at L = 25 uniformly distributed test points on a circle of radius 1 centred at the origin, for various numbers of degrees of freedom $M = N$ for the shapes (I)-(III).

| $M = N$ | $E$(bean) | $\mathcal{E}$(bean) | $E$(peach) | $\mathcal{E}$(peach) | $E$(peanut) | $\mathcal{E}$(peanut) |
|---|---|---|---|---|---|---|
| First Approach | | | | | | |
| 16 | 1.78(-4) | 8.28(-5) | 1.22(-3) | 4.68(-4) | 2.39(-2) | 1.03(-2) |
| 32 | 9.71(-7) | 3.61(-7) | 1.43(-7) | 5.59(-8) | 9.93(-4) | 3.65(-4) |
| 64 | 6.73(-14) | 3.06(-14) | 6.21(-12) | 2.42(-12) | 8.84(-8) | 3.30(-8) |
| Second Approach | | | | | | |
| 16 | 7.18(-4) | 2.63(-4) | 9.66(-4) | 3.18(-4) | 4.13(-2) | 1.52(-2) |
| 32 | 1.19(-6) | 5.15(-7) | 2.38(-7) | 7.86(-8) | 6.04(-4) | 2.22(-4) |
| 64 | 6.99(-13) | 2.64(-13) | 3.83(-12) | 1.39(-12) | 1.15(-7) | 5.13(-8) |
| Third Approach | | | | | | |
| 16 | 7.07(-3) | 2.98(-3) | 1.39(-3) | 7.27(-4) | 8.79(-3) | 3.70(-3) |
| 32 | 4.54(-6) | 1.62(-6) | 7.27(-7) | 2.37(-7) | 2.83(-4) | 1.08(-4) |
| 64 | 5.72(-12) | 1.96(-12) | 2.83(-14) | 1.45(-14) | 2.44(-7) | 9.10(-8) |
| Fourth Approach | | | | | | |
| 16 | 1.07(-4) | 4.00(-5) | 1.35(-4) | 4.33(-5) | 1.95(-2) | 7.26(-3) |
| 32 | 1.57(-7) | 6.26(-8) | 8.78(-8) | 2.77(-8) | 5.50(-4) | 2.22(-4) |
| 64 | 6.39(-14) | 2.71(-14) | 7.55(-15) | 2.48(-15) | 2.07(-7) | 7.71(-8) |

In Figures 2 and 3 we present the real and imaginary parts of the far field patterns of the reference solution and the numerical solution obtained using the third MFS approach (the results obtained with the fourth MFS approach were indistinguishable) with $M = N = 32$ for the smooth shapes (I)–(III), and with $M = N = 256$ for the non–smooth shapes (IV)-(V), respectively. Although not illustrated, excellent agreement with the corresponding BIM numerical results of [10] is reported. Also, in Tables 4 and 5 we list the errors $E$ and $\mathcal{E}$ obtained with different numbers of degrees of freedom for shapes (I)–(III) and (IV)–(V), respectively. We observe that, as expected, for the non–smooth shapes the convergence of the MFS with the number of degrees of freedom is considerably slower.

TABLE 3. Example 2: The maximum absolute error $E$ and the discrete $L^2$-error norm $\mathcal{E}$ between the exact solution (4.4) and the MFS approaches calculated at L = 25 uniformly distributed test points on a circle of radius 2 centred at the origin, for various numbers of degrees of freedom $M = N$ for the shapes (IV)-(V).

| $M = N$ | $E$(drop) | $\mathcal{E}$(drop) | $E$(heart) | $\mathcal{E}$(heart) |
|---|---|---|---|---|
| First approach | | | | |
| 16 | 1.41(-3) | 5.65(-4) | 2.09(-2) | 8.28(-3) |
| 32 | 1.25(-6) | 4.84(-7) | 1.07(-3) | 3.57(-4) |
| 64 | 1.03(-11) | 5.07(-12) | 1.79(-6) | 5.44(-7) |
| Second approach | | | | |
| 16 | 6.42(-4) | 2.86(-4) | 5.34(-3) | 2.34(-3) |
| 32 | 9.88(-7) | 4.70(-7) | 2.69(-4) | 1.03(-4) |
| 64 | 5.62(-11) | 2.12(-11) | 2.71(-7) | 8.57(-8) |
| Third approach | | | | |
| 16 | 9.43(-3) | 5.10(-3) | 1.01(-1) | 4.86(-2) |
| 32 | 2.02(-3) | 7.71(-4) | 8.69(-4) | 3.29(-4) |
| 64 | 7.33(-7) | 3.02(-7) | 3.21(-7) | 1.13(-7) |
| Fourth approach | | | | |
| 16 | 7.42(-5) | 4.00(-5) | 3.08(-2) | 1.25(-2) |
| 32 | 4.80(-7) | 2.17(-7) | 1.51(-4) | 5.88(-5) |
| 64 | 2.06(-10) | 7.55(-11) | 7.34(-7) | 2.37(-7) |

TABLE 4. Example 3: The maximum absolute error $E$ and the discrete $L^2$-error norm $\mathcal{E}$ between the reference solution and the third and fourth MFS approaches for the far-field pattern calculated at L = 32 uniformly distributed test points on the unit circle, for various numbers of degrees of freedom $M = N$ for the shapes (I)-(III).

| $M = N$ | $E$(bean) | $\mathcal{E}$(bean) | $E$(peach) | $\mathcal{E}$(peach) | $E$(peanut) | $\mathcal{E}$(peanut) |
|---|---|---|---|---|---|---|
| Third approach | | | | | | |
| 16 | 1.54(-1) | 1.00(-1) | 7.97(-2) | 4.41(-2) | 6.36(-2) | 4.38(-2) |
| 32 | 1.29(-2) | 7.96(-3) | 2.67(-4) | 1.52(-4) | 6.22(-3) | 4.43(-3) |
| 64 | 3.35(-4) | 1.65(-4) | 1.01(-7) | 5.47(-8) | 9.21(-8) | 7.22(-8) |
| 128 | 1.23(-6) | 6.27(-7) | 6.69(-9) | 3.59(-9) | 7.75(-14) | 4.90(-14) |
| Fourth approach | | | | | | |
| 16 | 1.02(-1) | 5.62(-2) | 2.85(-3) | 1.58 (-3) | 8.71(-3) | 5.99(-3) |
| 32 | 4.62(-2) | 2.72(-2) | 5.71(-5) | 3.41(-5) | 6.04(-4) | 2.22(-4) |
| 64 | 2.48(-4) | 1.21(-4) | 9.91(-8) | 5.37(-8) | 3.84(-9) | 2.69(-9) |
| 128 | 8.24(-6) | 4.32(-6) | 6.50(-9) | 3.48(-9) | 2.58(-13) | 1.37(-13) |

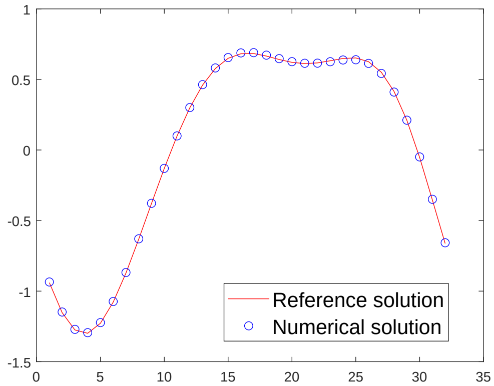


(a) Bean shape: Real part

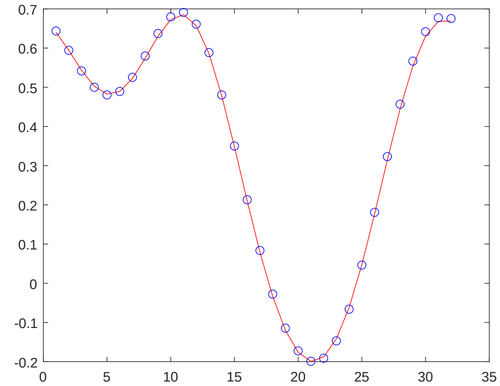

(b) Bean shape: Imaginary part

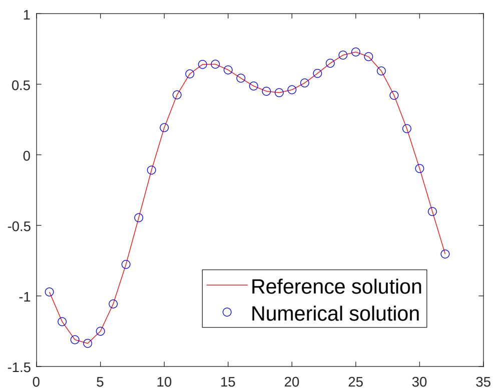


(c) Peach shape: Real part

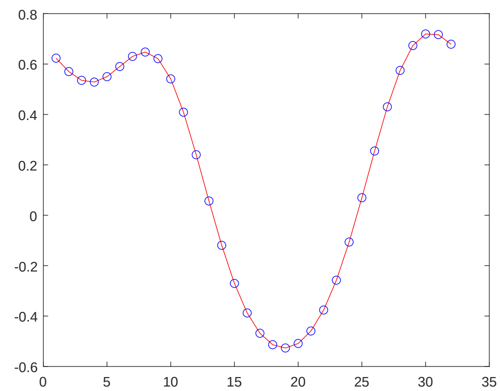

(d) Peach shape: Imaginary part

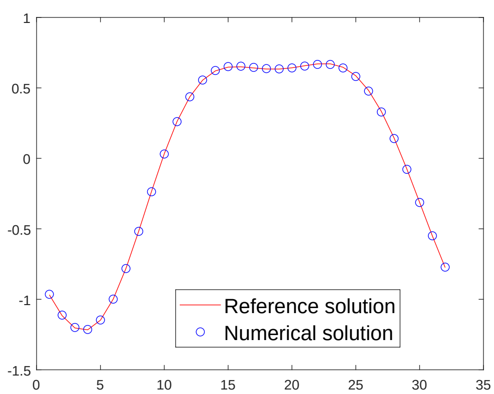


(e) Peanut shape: Real part

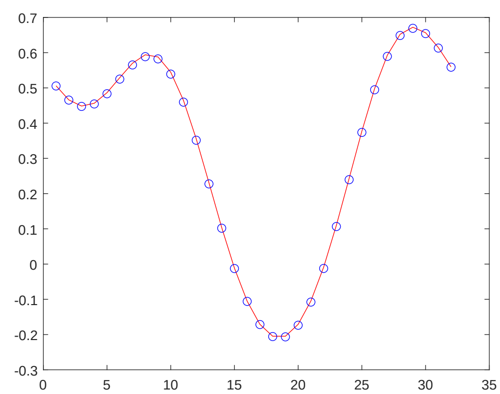

(f) Peanut shape: Imaginary part

FIGURE 2. Example 3: Real and imaginary parts of far–field patterns of reference and numerical solutions obtained using the third MFS approach with $M = N = 32$, for shapes (I)–(III).

TABLE 5. Example 3: The maximum absolute error $E$ and the discrete $L^2$-error norm $\mathcal{E}$ between the reference solution and the third and fourth MFS approaches for the far-field pattern calculated at L = 32 uniformly distributed test points on the unit circle, for various numbers of degrees of freedom $M = N$ for the shapes (IV)-(V).

| $M = N$ | $E$(drop) | $\mathcal{E}$(drop) | $E$(heart) | $\mathcal{E}$(heart) |
|---|---|---|---|---|
| Third approach | | | | |
| 128 | 4.14(-2) | 2.25(-2) | 9.30(+1) | 4.13(+1) |
| 256 | 8.27(-3) | 4.24(-3) | 4.66(-2) | 2.42(-2) |
| 512 | 4.09(-3) | 2.34(-3) | 3.33(-3) | 2.19(-3) |
| 1024 | 1.48(-3) | 8.41(-4) | 1.53(-3) | 9.61(-4) |
| Fourth approach | | | | |
| 128 | 3.27(-2) | 1.71(-2) | 6.01(+1) | 3.08(+1) |
| 256 | 8.60(-3) | 5.47(-3) | 2.07(-2) | 1.07(-2) |
| 512 | 4.37(-3) | 2.63(-3) | 4.66(-3) | 2.77(-3) |
| 1024 | 1.21(-3) | 8.15(-4) | 3.88(-3) | 2.09(-3) |

## 5. Inverse problem

The inverse problem in which the obstacle $D$ is unknown was investigated in [5] as a model arising in the non destructive testing of the fuselage or wing of an aircraft. We formulate the inverse geometric problem of detecting the obstacle $D$ in an infinite plate from suitable measurements, as proposed in [5]. We first assume that the unknown obstacle $D$ is contained in some *a priori* known disk $B_R(\mathbf{0})$ for some known radius $R > 0$. Then, for a point $\boldsymbol{y} \in \partial B_R(\mathbf{0}) =: \Gamma$, we denote by $v^{\mathrm{s}}(\cdot, \boldsymbol{y})$ and $\tilde{v}^{\mathrm{s}}(\cdot, \boldsymbol{y})$ the scattered fields associated with the incident point source and dipole fields

$$u^{\mathrm{inc}}(\cdot) = G(\cdot, \boldsymbol{y}) \tag{5.1}$$

and

$$u^{\mathrm{inc}}(\cdot) = \frac{\partial G}{\partial n(\boldsymbol{y})}(\cdot, \boldsymbol{y}), \tag{5.2}$$

where $\boldsymbol{n}(\boldsymbol{y})$ is the outward unit normal to $\Gamma$ at $\boldsymbol{y}$, respectively, via the corresponding solution of the direct problem (2.1)–(2.3). Note that unlike the direct problem where the incident field $u^{\mathrm{inc}}$ entering (2.3) was required to satisfy $\Delta^2 u^{\mathrm{inc}} - \kappa^4 u^{\mathrm{inc}} = 0$ in $\mathbb{R}^2$, see [4], in the inverse problem the incident field is required to satisfy $\Delta^2 u^{\mathrm{inc}} - \kappa^4 u^{\mathrm{inc}} = 0$ only in a domain including $\overline{D}$, see [5]. The resulting compound of measured data

$$v^{\mathrm{s}}(\boldsymbol{x}, \boldsymbol{y}) = f(\boldsymbol{x}, \boldsymbol{y}), \quad (\boldsymbol{x}, \boldsymbol{y}) \in \Gamma \times \Gamma, \tag{5.3}$$

$$\frac{\partial v^{\mathrm{s}}}{\partial n(\boldsymbol{x})}(\boldsymbol{x}, \boldsymbol{y}) = g(\boldsymbol{x}, \boldsymbol{y}), \quad (\boldsymbol{x}, \boldsymbol{y}) \in \Gamma \times \Gamma, \tag{5.4}$$

$$\tilde{v}^{\mathrm{s}}(\boldsymbol{x}, \boldsymbol{y}) = \tilde{f}(\boldsymbol{x}, \boldsymbol{y}), \quad (\boldsymbol{x}, \boldsymbol{y}) \in \Gamma \times \Gamma, \tag{5.5}$$

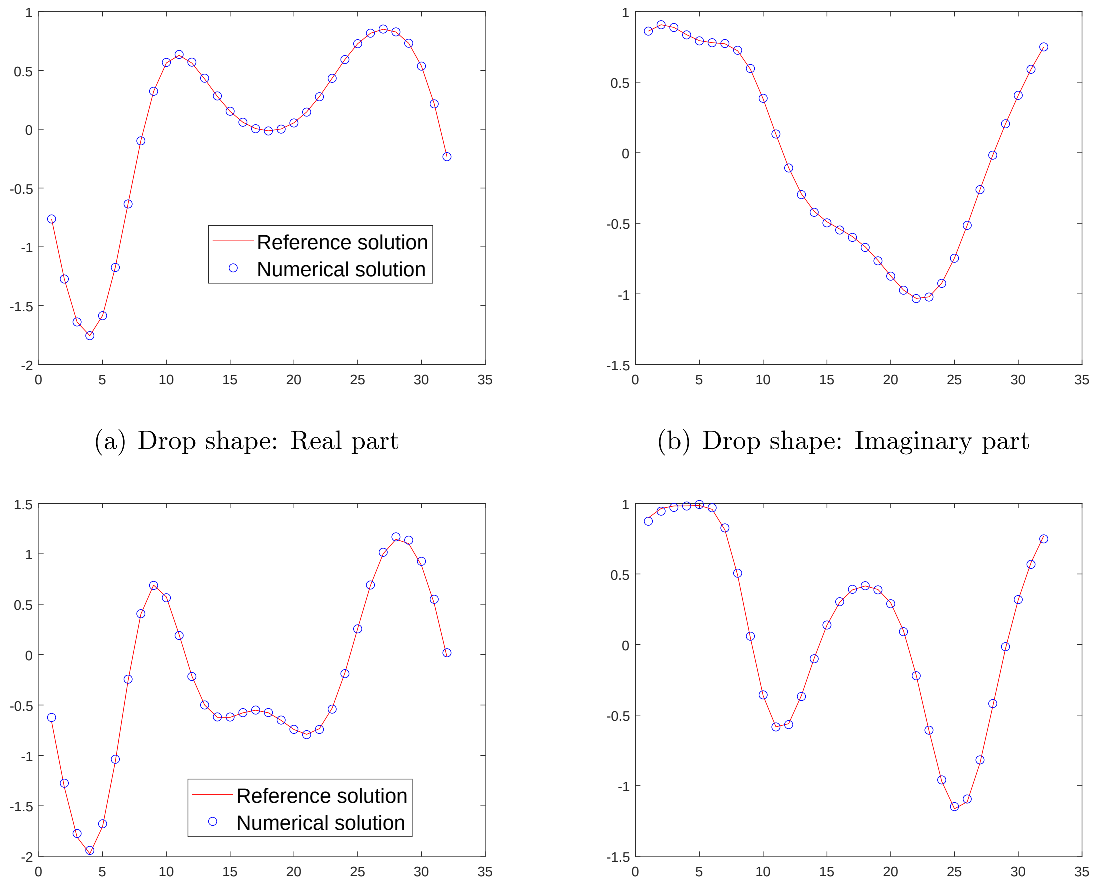


(a) Drop shape: Real part (b) Drop shape: Imaginary part

(c) Heart shape: Real part (d) Heart shape: Imaginary part

FIGURE 3. Example 3: Real and imaginary parts of far–field patterns of reference and numerical solutions obtained using the third MFS approach with $M = N = 256$, for shapes (IV)–(V).

$$\frac{\partial \tilde{v}^{\mathrm{s}}}{\partial n(\boldsymbol{x})}(\boldsymbol{x},\boldsymbol{y}) = \tilde{g}(\boldsymbol{x},\boldsymbol{y}), \quad (\boldsymbol{x},\boldsymbol{y}) \in \Gamma \times \Gamma, \tag{5.6}$$

called multistatic data, was shown to be sufficient for retrieving the obstacle $D$ uniquely for both the Dirichlet clamped plates and the Neumann free plates, see [4, Theorem 2.3]. In [4], the linear sampling method (LSM) was developed for identifying the cavity $D$ from the data (5.3)–(5.6). In the present paper, we develop a nonlinear Tikhonov regularization MFS for solving the inverse problem which is more precise and natural for solving nonlinear and ill–posed obstacle identification problems [16, 17].

5.1. **Numerical method for identification of cavity $D$.** We first assume that the unknown cavity $D \subset \mathbb{R}^2$ is star–shaped with respect to the origin and its boundary $\partial D$ parameterized by (3.3), where the polar radius $r(\vartheta)$ for $\vartheta \in [0, 2\pi)$ is a smooth $2\pi$–periodic function, which is unknown. For simplicity, we consider only the clamped boundary condition case (i) given by

$$v^{\mathrm{s}} = -u^{\mathrm{inc}}, \quad \frac{\partial v^{\mathrm{s}}}{\partial n} = -\frac{\partial u^{\mathrm{inc}}}{\partial n} \quad \text{on} \quad \partial D, \tag{5.7}$$

but a similar analysis can be performed for the free plate boundary conditions (iv). We shall use the Fourth MFS Approach and the first step is to fabricate the input data (5.3)–(5.6) that is required to be inverted in order to identify the obstacle (3.3). This is achieved numerically using the MFS approximation (3.16) with the sources $\left(\boldsymbol{\xi}_j\right)_{j=\overline{1,N}}$ distributed as in (3.10), which satisfies the governing equation (2.1) and the infinity condition (2.2). For each $\boldsymbol{y} \in \Gamma$, the unknown coefficients $(c_j)_{j=\overline{1,N}}$ and $(d_j)_{j=\overline{1,N}}$ are determined by imposing the boundary conditions (5.7) for the point source incident field (5.1). Once these coefficients have been found, equation (3.16) applied on $\Gamma$ provides the data (5.3). Also, the differentiation of (3.16) and application on $\Gamma$ given by

$$\frac{\partial v_N^{\mathrm{s}}}{\partial n}(\boldsymbol{x}) = \sum_{j=1}^{N} c_j \, \frac{\partial G_{\mathrm{M}}}{\partial n(\boldsymbol{x})}(\boldsymbol{x}, \boldsymbol{\xi}_j) + \sum_{j=1}^{N} d_j \, \frac{\partial G_{\mathrm{H}}}{\partial n(\boldsymbol{x})}(\boldsymbol{x}, \boldsymbol{\xi}_j), \quad \boldsymbol{x} \in \Gamma, \tag{5.8}$$

where

$$\frac{\partial G_{\mathrm{M}}}{\partial n(\boldsymbol{x})}(\boldsymbol{x}, \boldsymbol{\xi}_j) = \frac{\kappa \left(\boldsymbol{x} - \boldsymbol{\xi}_j\right) \cdot \boldsymbol{n}(\boldsymbol{x})}{4|\boldsymbol{x} - \boldsymbol{\xi}_j|} \, H_1^{(1)}(\mathrm{i}\kappa|\boldsymbol{x} - \boldsymbol{\xi}_j|),$$
$$\frac{\partial G_{\mathrm{H}}}{\partial n(\boldsymbol{x})}(\boldsymbol{x}, \boldsymbol{\xi}_j) = -\frac{\mathrm{i}\kappa \left(\boldsymbol{x} - \boldsymbol{\xi}_j\right) \cdot \boldsymbol{n}(\boldsymbol{x})}{4|\boldsymbol{x} - \boldsymbol{\xi}_j|} \, H_1^{(1)}(\kappa|\boldsymbol{x} - \boldsymbol{\xi}_j|),$$

provide the data (5.4). The procedure is repeated for the dipole incident field (5.2) to provide the data (5.5) and (5.6).

On choosing the points

$$\boldsymbol{Y}_k = \boldsymbol{X}_k = R\left(\cos\varphi_k, \sin\varphi_k\right), \quad \varphi_k = 2\pi(k-1)/K, \quad k = \overline{1, K}, \tag{5.9}$$

on $\Gamma$, each of the data (5.3)–(5.6) generate a full matrix multistatic data compound given by

$$\mathrm{F} = \left(f(\boldsymbol{X}_k, \boldsymbol{Y}_\ell)\right)_{k,\ell=\overline{1,K}}, \quad \mathrm{G} = \left(g(\boldsymbol{X}_k, \boldsymbol{Y}_\ell)\right)_{k,\ell=\overline{1,K}},$$
$$\widetilde{\mathrm{F}} = \left(\tilde{f}(\boldsymbol{X}_k, \boldsymbol{Y}_\ell)\right)_{k,\ell=\overline{1,K}}, \quad \widetilde{\mathrm{G}} = \left(\tilde{g}(\boldsymbol{X}_k, \boldsymbol{Y}_\ell)\right)_{k,\ell=\overline{1,K}}.$$

Summing up, the whole inverse model consists of the following assembly of discretized equations resulting from (5.8) applied for $u^{\mathrm{inc}}$ given by (5.1) and (5.2), and equations (5.3)–(5.6):

$$\sum_{j=1}^{N} c_j(\boldsymbol{Y}_\ell) G_{\mathrm{M}}\left((r_m\cos\tilde{\vartheta}_m, r_m\sin\tilde{\vartheta}_m), \boldsymbol{\xi}_j\right) + \sum_{j=1}^{N} d_j(\boldsymbol{Y}_\ell) G_{\mathrm{H}}\left((r_m\cos\tilde{\vartheta}_m, r_m\sin\tilde{\vartheta}_m), \boldsymbol{\xi}_j\right)$$
$$+ G\left((r_m\cos\tilde{\vartheta}_m, r_m\sin\tilde{\vartheta}_m), \boldsymbol{Y}_\ell\right) = 0, \quad m = \overline{1, M}, \; \ell = \overline{1, K}, \tag{5.10}$$

$$\sum_{j=1}^{N} c_j(\boldsymbol{Y}_\ell)\frac{\partial G_{\mathrm{M}}}{\partial n(\boldsymbol{x})}\Big((r_m\cos\tilde{\vartheta}_m, r_m\sin\tilde{\vartheta}_m),\boldsymbol{\xi}_j\Big) + \sum_{j=1}^{N} d_j(\boldsymbol{Y}_\ell)\frac{\partial G_{\mathrm{H}}}{\partial n(\boldsymbol{x})}\Big((r_m\cos\tilde{\vartheta}_m, r_m\sin\tilde{\vartheta}_m),\boldsymbol{\xi}_j\Big)$$
$$+\frac{\partial G}{\partial n(\boldsymbol{x})}\Big((r_m\cos\tilde{\vartheta}_m, r_m\sin\tilde{\vartheta}_m),\boldsymbol{Y}_\ell\Big) = 0, \quad m=\overline{1,M},\ \ell=\overline{1,K}, \tag{5.11}$$

$$\sum_{j=1}^{N} c_j(\boldsymbol{Y}_\ell)G_{\mathrm{M}}\left(\boldsymbol{X}_k,\boldsymbol{\xi}_j\right) + \sum_{j=1}^{N} d_j(\boldsymbol{Y}_\ell)G_{\mathrm{H}}\left(\boldsymbol{X}_k,\boldsymbol{\xi}_j\right) = f(\boldsymbol{X}_k,\boldsymbol{Y}_\ell), \quad k,\ell=\overline{1,K}, \tag{5.12}$$

$$\sum_{j=1}^{N} c_j(\boldsymbol{Y}_\ell)\frac{\partial G_{\mathrm{M}}}{\partial n(\boldsymbol{x})}\left(\boldsymbol{X}_k,\boldsymbol{\xi}_j\right) + \sum_{j=1}^{N} d_j(\boldsymbol{Y}_\ell)\frac{\partial G_{\mathrm{H}}}{\partial n(\boldsymbol{x})}\left(\boldsymbol{X}_k,\boldsymbol{\xi}_j\right) = g(\boldsymbol{X}_k,\boldsymbol{Y}_\ell), \quad k,\ell=\overline{1,K}, \tag{5.13}$$

$$\sum_{j=1}^{N} \tilde{c}_j(\boldsymbol{Y}_\ell)G_{\mathrm{M}}\Big((r_m\cos\tilde{\vartheta}_m, r_m\sin\tilde{\vartheta}_m),\boldsymbol{\xi}_j\Big) + \sum_{j=1}^{N} \tilde{d}_j(\boldsymbol{Y}_\ell)G_{\mathrm{H}}\Big((r_m\cos\tilde{\vartheta}_m, r_m\sin\tilde{\vartheta}_m),\boldsymbol{\xi}_j\Big)$$
$$+\frac{\partial G}{\partial n(\boldsymbol{y})}\Big((r_m\cos\tilde{\vartheta}_m, r_m\sin\tilde{\vartheta}_m),\boldsymbol{Y}_\ell\Big) = 0, \quad m=\overline{1,M},\ \ell=\overline{1,K}, \tag{5.14}$$

$$\sum_{j=1}^{N} \tilde{c}_j(\boldsymbol{Y}_\ell)\frac{\partial G_{\mathrm{M}}}{\partial n(\boldsymbol{x})}\Big((r_m\cos\tilde{\vartheta}_m, r_m\sin\tilde{\vartheta}_m),\boldsymbol{\xi}_j\Big) + \sum_{j=1}^{N} \tilde{d}_j(\boldsymbol{Y}_\ell)\frac{\partial G_{\mathrm{H}}}{\partial n(\boldsymbol{x})}\Big((r_m\cos\tilde{\vartheta}_m, r_m\sin\tilde{\vartheta}_m),\boldsymbol{\xi}_j\Big)$$
$$+\frac{\partial^2 G}{\partial n(\boldsymbol{x})\partial n(\boldsymbol{y})}\Big((r_m\cos\tilde{\vartheta}_m, r_m\sin\tilde{\vartheta}_m),\boldsymbol{Y}_\ell\Big) = 0, \quad m=\overline{1,M},\ \ell=\overline{1,K}, \tag{5.15}$$

$$\sum_{j=1}^{N} \tilde{c}_j(\boldsymbol{Y}_\ell)G_{\mathrm{M}}\left(\boldsymbol{X}_k,\boldsymbol{\xi}_j\right) + \sum_{j=1}^{N} \tilde{d}_j(\boldsymbol{Y}_\ell)G_{\mathrm{H}}\left(\boldsymbol{X}_k,\boldsymbol{\xi}_j\right) = \tilde{f}(\boldsymbol{X}_k,\boldsymbol{Y}_\ell), \quad k,\ell=\overline{1,K}, \tag{5.16}$$

$$\sum_{j=1}^{N} \tilde{c}_j(\boldsymbol{Y}_\ell)\frac{\partial G_{\mathrm{M}}}{\partial n(\boldsymbol{x})}\left(\boldsymbol{X}_k,\boldsymbol{\xi}_j\right) + \sum_{j=1}^{N} \tilde{d}_j(\boldsymbol{Y}_\ell)\frac{\partial G_{\mathrm{H}}}{\partial n(\boldsymbol{x})}\left(\boldsymbol{X}_k,\boldsymbol{\xi}_j\right) = \tilde{g}(\boldsymbol{X}_k,\boldsymbol{Y}_\ell), \quad k,\ell=\overline{1,K}, \tag{5.17}$$

where $r_m := r(\tilde{\vartheta}_m)$, $m=\overline{1,M}$. Along with $c_{j\ell} := c_j(\boldsymbol{Y}_\ell)$, $d_{j\ell} := d_j(\boldsymbol{Y}_\ell)$, $\tilde{c}_{j\ell} := \tilde{c}_j(\boldsymbol{Y}_\ell)$ and $\tilde{d}_{j\ell} := \tilde{d}_j(\boldsymbol{Y}_\ell)$, for $j=\overline{1,N}, \ell=\overline{1,K}$, this amounts to $M+4NK$ unknowns entering the $4MK+4K^2$ equations (5.10)–(5.17). This system of nonlinear algebraic equations is solved by minimizing the least–squares residual penalised by the first–order regularizing term of the form $\lambda\sum_{m=1}^{M}\left(r_{m+1}-r_m\right)^2$, where $\lambda\geq 0$ is a regularization parameter to be prescribed and, by convention $r_{M+1}=r_1$, which implies $C^1$–smoothness of the cavity $D$. The resulting nonlinear Tikhonov regularization functional is given by

$$\mathcal{T}_\lambda(\mathrm{C},\mathrm{D},\widetilde{\mathrm{C}},\widetilde{\mathrm{D}},\boldsymbol{r}) := ||\mathcal{F}(\mathrm{C},\mathrm{D},\widetilde{\mathrm{C}},\widetilde{\mathrm{D}},\boldsymbol{r})-\boldsymbol{b}||^2 + \lambda\sum_{m=1}^{M}\left(r_{m+1}-r_m\right)^2, \tag{5.18}$$

where

$$\mathrm{C}=\left(c_{j\ell}\right)_{j=\overline{1,N},\ell=\overline{1,K}}, \quad \mathrm{D}=\left(d_{j\ell}\right)_{j=\overline{1,N},\ell=\overline{1,K}}, \quad \widetilde{\mathrm{C}}=\left(\tilde{c}_{j\ell}\right)_{j=\overline{1,N},\ell=\overline{1,K}}, \quad \widetilde{\mathrm{D}}=\left(\tilde{d}_{j\ell}\right)_{j=\overline{1,N},\ell=\overline{1,K}},$$

$\boldsymbol{r} = (r_m)_{m=\overline{1,M}}$ , $\boldsymbol{b}$ is a vector of $4MK + 4K^2$ components containing the unknown data in the right–hand side of (5.10)–(5.17), and $\mathcal{F}(\mathrm{C}, \mathrm{D}, \widetilde{\mathrm{C}}, \widetilde{\mathrm{D}}, \boldsymbol{r})$ is the functional built by assembling the appropriate expressions in the left–hand side of (5.10)–(5.17). The minimization of (5.18) subject to the simple bounds

$$0 < r_m < R \quad \text{for} \quad m = \overline{1, M} \tag{5.19}$$

is performed using the MATLAB® toolbox routine `lsqnonlin`, which has proved a versatile and easy to use software in several nonlinear minimizations resulting from solving numerically inverse and ill–posed problems, see e.g. [16–18].

**Remark**. The routine `lsqnonlin` minimizes the sum of squares of real equations in real unknowns. Hence, in the implementation, we need to provide it with the real and imaginary parts of the complex equations (5.10)–(5.17) leading to a total number of $2 \times (4MK + 4K^2)$ equations. Also, we need to consider the real and imaginary parts of the complex coefficients $c_{j\ell}$, $d_{j\ell}$, $\tilde{c}_{j\ell}$ and $\tilde{d}_{j\ell}$, for $j = \overline{1, N}, \ell = \overline{1, K}$, which in addition to the (real) radii $r_m$, $m = \overline{1, M}$, lead to a total number of $M + 2 \times (4NK)$ unknowns.

5.2. **Numerical implementation.** In the numerical implementation of the described method we consider the identification of a circular disk scatterer $D = B_1(\mathbf{0})$ of radius 1 centred at the origin from the measurements (5.3)–(5.6). We first fabricate the input data (5.3)–(5.6) using the Fourth MFS Approach given by expansion (3.16) in Section 3.4. We take $\kappa = 1$, and $M = N = 32$, $\eta = 0.5$. The results for the data (5.3)–(5.6) are given in Table 6 for $R = 2$ and $K = 2$. In the inverse problem we use this data as input in the inverse problem that we solve, as described in Section 5.1, and take $M = N = 16$ (which is different than the direct problem solver in order to avoid committing an inverse crime) and $\eta = 0.5$. This leads to a total of 288 (real) equations in 272 (real) unknowns.

With $M = N = 16$ and $K = 2$, equations (5.10)–(5.17) form a nonlinear system of $4MK + 4K^2 = 144$ equations with $M + 4NK = 144$ unknowns, which is solved by minimizing (5.18) subject to the constraints (5.19) from the initial guess $r_m^{(0)} = 0.5$ for $m = \overline{1, 16}$ and $\mathrm{C}^{(0)} = \mathrm{D}^{(0)} = \widetilde{\mathrm{C}}^{(0)} = \widetilde{\mathrm{D}}^{(0)} = 0$. The numerically obtained results without regularization, i.e. $\lambda = 0$, for the cavity $D$ are illustrated in Figure 4 for various numbers of iterations showing convergent and accurate reconstructions.

Next, in order to test the stability of the numerical reconstruction we perturb the data (5.3)–(5.6) of Table 6 by replacing $f(\boldsymbol{X}_k, \boldsymbol{Y}_\ell)$ with $(1+p\,\varrho_{k,\ell})f(\boldsymbol{X}_k, \boldsymbol{Y}_\ell)$, $k, \ell = \overline{1, K}$, where $p$ is the percentage noise added and $[\varrho_{1,1}, \varrho_{1,2}, \ldots, \varrho_{1,K}, \varrho_{2,1}, \ldots, \varrho_{2,K}, \ldots, \varrho_{K,K}]^T$ is a random noisy variable vector with components in [-1,1] obtained via the MATLAB® command `-1+2*rand(1,`$K$`)`. Similarly for $g, \tilde{f}, \tilde{g}$. Figure 5 presents the numerically retrieved cavity after 200 iterations for $p = 5\%$ and various values of $\lambda$. From this figure it can be seen that stable and accurate reconstructions of the cavity can be achieved by a suitable choice of the regularization parameter, e.g. $\lambda = \lambda(5\%)$ between $10^2$ and $10^3$.

Table 6. The data (5.3)–(5.6) fabricated by solving the direct problem using the fourth MFS approach with $M = N = 32$ and $\eta = 0.5$.

| $(\boldsymbol{X}_k, \boldsymbol{Y}_\ell)$ | $f$ | $g$ | $\tilde{f}$ | $\tilde{g}$ |
|---|---|---|---|---|
| $(\boldsymbol{X}_1, \boldsymbol{Y}_1) = ((2,0),(2,0))$ | 0.0644-0.0868i | 0.0371+0.0508i | 0.0371+0.0508i | -0.0335+0.0054i |
| $(\boldsymbol{X}_1, \boldsymbol{Y}_2) = ((2,0),(-2,0))$ | -0.0011+0.0500i | -0.0507-0.0077i | -0.0507-0.0077i | 0.0155-0.0469i |
| $(\boldsymbol{X}_2, \boldsymbol{Y}_1) = ((-2,0),(2,0))$ | -0.0011+0.0500 i | -0.0507-0.0077i | -0.0507-0.0077i | 0.0155-0.0469i |
| $(\boldsymbol{X}_2, \boldsymbol{Y}_2) = ((-2,0),(-2,0))$ | 0.0644-0.0868i | 0.0371+0.0508i | 0.0371+0.0508i | -0.0335+0.0054i |

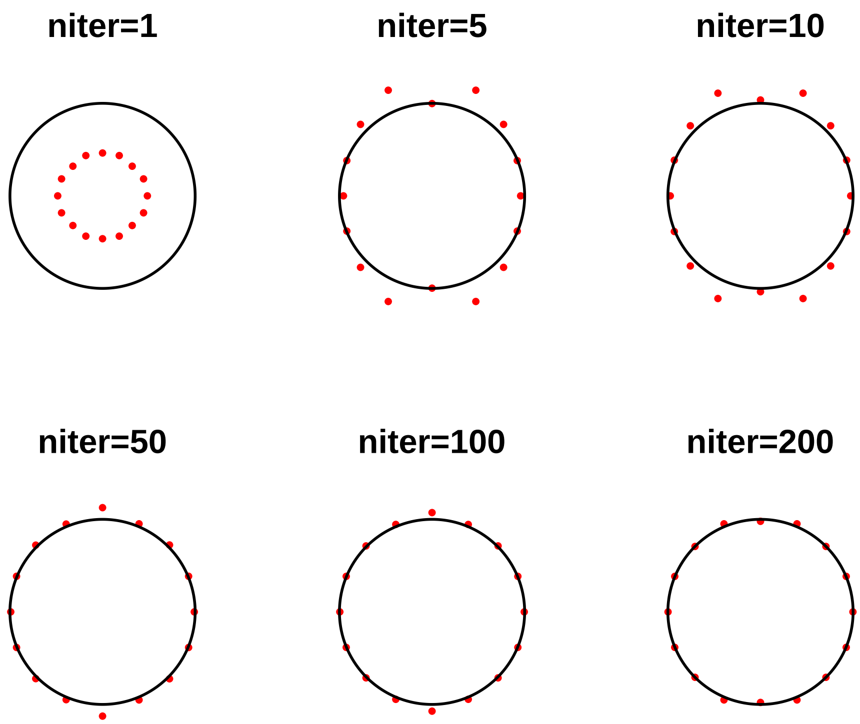


Figure 4. Results. The reconstructed cavity (red dots) after various numbers of iterations, no noise and no regularization.

## 6. Conclusions

In this paper, the MFS has been developed for the first time in the relevant literature for solving both direct and inverse scattering problems from infinite elastic thin plates. In this practical scenario the bi–Laplacian of the scattered field is augmented by a lower–order term.

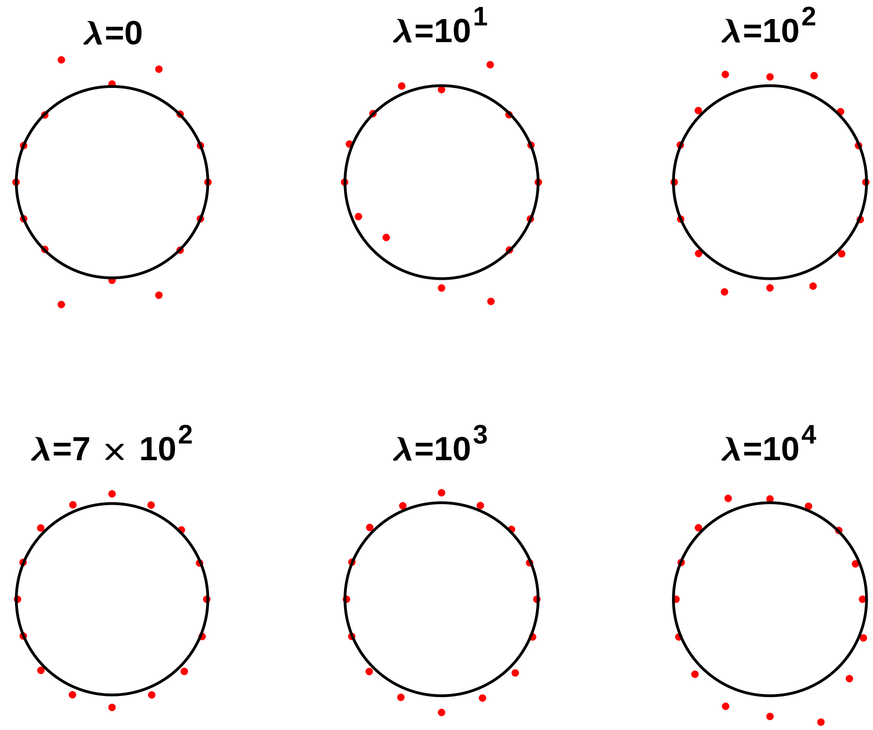


FIGURE 5. The reconstructed cavity (red dots) after 200 iterations for various values of the regularization parameter $\lambda$ and noise $p = 5\%$.

Four variants of the MFS have been investigated. From the results reported in Section 4, the performance of all four approaches with respect to accuracy is similar when compared with the analytical solutions available for Examples 1 and 2, or with a reference solution or the BIM numerical results of [10] for Example 3, which does not possess an explicitly available analytical solution. From the ease of implementation standpoint, clearly the first approach (described in Section 3.1) is the simplest as the approximation involves only one fundamental solution (basis function). However, in contrast to the other three approaches (described in Sections 3.2–3.4), the drawback is that two pseudo–boundaries instead of one need to be chosen. As elaborated at the beginning of Section 4, this is not such a serious drawback as, provided that the choices are reasonable, the position(s) of the pseudo–boundary(ies) do not significantly affect the solution's accuracy. The second and third approaches are potentially more tedious to implement due to the presence of the (extra) derivatives in expressions (3.9) and (3.12), especially in cases where the boundary condition operators $\mathcal{B}_1$ and $\mathcal{B}_2$ in (2.3) involve higher-order derivatives, rendering the coefficient matrices resulting from these two approaches more vulnerable to ill–conditioning. We should also mention that all four proposed approaches are considerably simpler than their BIM counterparts as they are meshless and do not involve troublesome integrations.

As for the inverse analysis undertaken in Section 5, the identification of an unknown cavity concealed in an infinite plate has been accomplished by the fourth MFS approach combined with a constrained minimization embedded in the MATLAB® routine `lsqnonlin`. The numerical results obtained for both exact and noisy input near–field multistatic data reveal satisfactorily stable and accurate reconstructions.

**Acknowledgments.** No data are associated with this article. For the purpose of open access, the authors have applied a Creative Commons Attribution (CC BY) licence to any Author Accepted Manuscript version arising from this submission.

## References

[1] M. Abramowitz and I. A. Stegun, *Handbook of Mathematical Functions*, Dover, New York, 1965.
[2] C. J. S. Alves, *Density results for the Helmholtz equation and the method of fundamental solutions*, In: Advances in Computational Engineering & Sciences, (eds. S. N. Atluri and F. W. Burst), Vol. I, Tech Science Press, pp. 45–50, 2000.
[3] C. J. S. Alves and P. M. C. Ribeiro, *Crack detection using spherical incident waves and near–field measurements*, in Boundary Elements XXI, (eds. C. A. Brebbia and H. Power), WIT Press, Southampton, pp. 355–364, 1999.
[4] L. Bourgeois and C. Hazard, *On well–posedness of scattering problems in a Kirchhoff–Love infinite plate*, SIAM J. Appl. Math., **80** (2020), 1546–1566.
[5] L. Bourgeois and A. Recoquillay, *The linear sampling method for Kirchhoff–Love infinite plates*, Inverse Probl. Imaging, **14** (2020), 363–384.
[6] C. S. Chen, A. Karageorghis and Y. Li, *On choosing the location of the sources in the MFS*, Numer. Algorithms, **72** (2016), 107–130.
[7] Z. Chen and F. Wang, *Localized method of fundamental solutions for acoustic analysis inside a car cavity with sound–absorbing material*, Adv. Appl. Math. Mech., **15** (2023), 182–201.
[8] Z. Chen, F. Wang, S. Cheng and G. Wu, *Localized MFS for three–dimensional acoustic inverse problems on complicated domains*, Int. J. Mech. Syst. Dyn., **2** (2022), 143–152.
[9] D. Colton and R. Kress, *Inverse Acoustic and Electromagnetic Scattering Theory*, 4th edition, Springer, Berlin, 2019.
[10] H. Dong and P. Li, *A novel boundary integral formulation for the biharmonic wave scattering problem*, J. Sci. Comput., **98** (2024), Article No. 42, (29 pages).
[11] D. V. Evans and R. Porter, *Penetration of flexural waves through a periodically constrained thin elastic plate in vacuo and floating on water*, J. Eng. Math., **58** (2007), 317–337.
[12] G. Fairweather, A. Karageorghis and P. A. Martin, *The method fundamental solutions for scattering and radiation problems*, Eng. Anal. Bound. Elem., **27** (2003), 759–769.
[13] Z. Fu and W. Chen, *A truly boundary-only meshfree method applied to Kirchhoff plate bending problems*, Adv. Appl. Math. Mech., **1** (2009), 341–352.
[14] Z. Fu, W. Chen and W. Yang, *Winkler plate bending problems by a truly boundary-only boundary particle method*, Comput. Mech., **44** (2009), 757–763.
[15] G. C. Hsiao and W. L. Wendland, *Boundary Integral Equations*, Springer–Verlag, Berlin, 2008.
[16] A. Karageorghis and D. Lesnic, *Application of the MFS to inverse scattering problems*, Eng. Anal. Bound. Elem., **35** (2011), 631–638.

[17] A. Karageorghis, D. Lesnic and L. Marin, *The MFS for the identification of a sound–soft interior acoustic scatterer*, Eng. Anal. Bound. Elem., **83** (2017), 107–112.
[18] A. Karageorghis, D. Lesnic and L. Marin, *The method of fundamental solutions for the identification of a scatterer with impedance boundary condition in interior acoustic scattering*, Eng. Anal. Bound. Elem., **92** (2017), 218–224.
[19] A. Mohsen, *The source simulation technique for exterior problems in acoustics*, ZAMP, **43** (1992), 401–404.
[20] Y. Niwa, S. Kobayashi and M. Kitahara, *Eigenfrequency analysis of a plate by the integral equation method*, Theor. Appl. Mech., **29** (1981), 287–307.
[21] A. N. Norris and C. Vemula, *Scattering of flexural waves on thin plates*, J. Sound Vib., **181** (1995), 115–125.
[22] W. J. Parnell and P. A. Martin, *Multiple scattering of flexural waves by configurations of inclusions in thin plates*, Wave Motion, **48** (2011), 161–175.
[23] C. Providakis and D. Beskos, *Dynamic analysis of plates by boundary elements*, Appl. Mech. Rev., **52** (1999), 213–236.
[24] M. J. A. Smith, M. H. Meylon and R. C. McPhedron, *Scattering by cavities of arbitrary shape in an infinite plate and associated vibration problems*, J. Sound Vib., **330** (2011), 4029–4046.
[25] Y.-S. Smyrlis and A. Karageorghis, *Efficient implementation of the MFS: The three scenarios*, J. Comput. Appl. Math., **227** (2009), 83–92.
[26] N. Stinger, M. Wilhelm and M. Wegener, *Experiments on elastic cloacking in thin plates*, Phys. Rev. Lett., **108** (2012), Article No. 014301.
[27] J. Vivoli and P. Filippi, *Eigenfrequencies of thin plates and layered potentials*, J. Acoust. Soc. Am., **55** (1974), 562–567.
[28] F. Wang, C-M. Fan, Q. Hua and Y. Gu, *Localized MFS for the inverse Cauchy problems of two–dimensional Laplace and biharmonic equations*, Appl. Math. Comput., **364** (2020), Article No. 124658, (14 pages).
[29] P. H. Wen, *Point intensity method of solving circular plate resting on elastical subgrade*, Eng. Mech., **4** (1987), 18–26.

## Appendix

We shall be repeatedly employing the identity [1]

$$\frac{d}{dz} H_{\mathsf{n}}^{(1)}(z) = \frac{\mathsf{n} H_{\mathsf{n}}^{(1)}(z)}{z} - H_{\mathsf{n}+1}^{(1)}(z),$$

and for the evaluation of the Hankel function $H_{\mathsf{n}}^{(1)}(z)$ we used the MATLAB® command `besselh(n,z)`. To impose the boundary conditions (2.3) in (i) and (ii) we need the following derivatives:

**First Approach.**

$$\frac{\partial G}{\partial x_j}(\boldsymbol{x}, \boldsymbol{\xi}) = -\frac{\mathrm{i}(x_j - \xi_j)}{8\kappa|\boldsymbol{x} - \boldsymbol{\xi}|} \left[ H_1^{(1)}(\kappa|\boldsymbol{x} - \boldsymbol{\xi}|) - \mathrm{i} H_1^{(1)}(\mathrm{i}\kappa|\boldsymbol{x} - \boldsymbol{\xi}|) \right], \quad j = 1, 2,$$

$$\frac{\partial^2 G}{\partial x_1^2}(\boldsymbol{x}, \boldsymbol{\xi}) = -\frac{1}{8\kappa|\boldsymbol{x} - \boldsymbol{\xi}|} \left[ \mathrm{i} H_1^{(1)}(\kappa|\boldsymbol{x} - \boldsymbol{\xi}|) + H_1^{(1)}(\mathrm{i}\kappa|\boldsymbol{x} - \boldsymbol{\xi}|) \right]$$

$$+\frac{\mathrm{i}(x_1 - \xi_1)^2}{8|\boldsymbol{x} - \boldsymbol{\xi}|^2} \left[ H_2^{(1)}(\kappa|\boldsymbol{x} - \boldsymbol{\xi}|) + H_2^{(1)}(\mathrm{i}\kappa|\boldsymbol{x} - \boldsymbol{\xi}|) \right],$$

$$\frac{\partial^2 G}{\partial x_2^2}(\boldsymbol{x}, \boldsymbol{\xi}) = -\frac{1}{8\kappa|\boldsymbol{x} - \boldsymbol{\xi}|} \left[ \mathrm{i} H_1^{(1)}(\kappa|\boldsymbol{x} - \boldsymbol{\xi}|) + H_1^{(1)}(\mathrm{i}\kappa|\boldsymbol{x} - \boldsymbol{\xi}|) \right]$$

$$+\frac{\mathrm{i}(x_2-\xi_2)^2}{8|\boldsymbol{x}-\boldsymbol{\xi}|^2}\left[H_2^{(1)}(\kappa|\boldsymbol{x}-\boldsymbol{\xi}|)+H_2^{(1)}(\mathrm{i}\kappa|\boldsymbol{x}-\boldsymbol{\xi}|)\right],$$

$$\frac{\partial^2 G}{\partial x_1 \partial x_2}(\boldsymbol{x},\boldsymbol{\xi}) = \frac{\mathrm{i}(x_1-\xi_1)(x_2-\xi_2)}{8|\boldsymbol{x}-\boldsymbol{\xi}|^2}\left[H_2^{(1)}(\kappa|\boldsymbol{x}-\boldsymbol{\xi}|)+H_2^{(1)}(\mathrm{i}\kappa|\boldsymbol{x}-\boldsymbol{\xi}|)\right],$$

where $\boldsymbol{x}=(x_1,x_2)$ and $\boldsymbol{\xi}=(\xi_1,\xi_2)$.

**Second Approach.**

$$\frac{\partial G}{\partial \xi_j}(\boldsymbol{x},\boldsymbol{\xi}) = \frac{\mathrm{i}(x_j-\xi_j)}{8\kappa|\boldsymbol{x}-\boldsymbol{\xi}|}\left[H_1^{(1)}(\kappa|\boldsymbol{x}-\boldsymbol{\xi}|)-\mathrm{i}H_1^{(1)}(\mathrm{i}\kappa|\boldsymbol{x}-\boldsymbol{\xi}|)\right], \quad j=1,2,$$

$$\frac{\partial^2 G}{\partial \xi_1 \partial x_1}(\boldsymbol{x},\boldsymbol{\xi}) = \frac{1}{8\kappa|\boldsymbol{x}-\boldsymbol{\xi}|}\left[\mathrm{i}H_1^{(1)}(\kappa|\boldsymbol{x}-\boldsymbol{\xi}|)+H_1^{(1)}(\mathrm{i}\kappa|\boldsymbol{x}-\boldsymbol{\xi}|)\right]$$

$$-\frac{\mathrm{i}(x_1-\xi_1)^2}{8|\boldsymbol{x}-\boldsymbol{\xi}|^2}\left[H_2^{(1)}(\kappa|\boldsymbol{x}-\boldsymbol{\xi}|)+H_2^{(1)}(\mathrm{i}\kappa|\boldsymbol{x}-\boldsymbol{\xi}|)\right],$$

$$\frac{\partial^2 G}{\partial \xi_2 \partial x_2}(\boldsymbol{x},\boldsymbol{\xi}) = \frac{1}{8\kappa|\boldsymbol{x}-\boldsymbol{\xi}|}\left[\mathrm{i}H_1^{(1)}(\kappa|\boldsymbol{x}-\boldsymbol{\xi}|)+H_1^{(1)}(\mathrm{i}\kappa|\boldsymbol{x}-\boldsymbol{\xi}|)\right]$$

$$-\frac{\mathrm{i}(x_2-\xi_2)^2}{8|\boldsymbol{x}-\boldsymbol{\xi}|^2}\left[H_2^{(1)}(\kappa|\boldsymbol{x}-\boldsymbol{\xi}|)+H_2^{(1)}(\mathrm{i}\kappa|\boldsymbol{x}-\boldsymbol{\xi}|)\right],$$

$$\frac{\partial^2 G}{\partial \xi_1 \partial x_2}(\boldsymbol{x},\boldsymbol{\xi}) = \frac{\partial^2 G}{\partial \xi_2 \partial x_1}(\boldsymbol{x},\boldsymbol{\xi}) = -\frac{\mathrm{i}(x_1-\xi_1)(x_2-\xi_2)}{8|\boldsymbol{x}-\boldsymbol{\xi}|^2}\left[H_2^{(1)}(\kappa|\boldsymbol{x}-\boldsymbol{\xi}|)+H_2^{(1)}(\mathrm{i}\kappa|\boldsymbol{x}-\boldsymbol{\xi}|)\right].$$

**Third Approach.**

$$\frac{\partial G_{\mathrm{M}}}{\partial x_j}(\boldsymbol{x},\boldsymbol{\xi}) = \frac{\kappa(x_j-\xi_j)}{4|\boldsymbol{x}-\boldsymbol{\xi}|}H_1^{(1)}(\mathrm{i}\kappa|\boldsymbol{x}-\boldsymbol{\xi}|), \quad j=1,2,$$

$$\frac{\partial G_{\mathrm{H}}}{\partial \xi_j}(\boldsymbol{x},\boldsymbol{\xi}) = -\frac{\mathrm{i}\kappa(x_j-\xi_j)}{4|\boldsymbol{x}-\boldsymbol{\xi}|}H_1^{(1)}(\kappa|\boldsymbol{x}-\boldsymbol{\xi}|), \quad j=1,2,$$

$$\frac{\partial^2 G_{\mathrm{H}}}{\partial \xi_1 \partial x_1}(\boldsymbol{x},\boldsymbol{\xi}) = -\frac{\mathrm{i}\kappa}{4|\boldsymbol{x}-\boldsymbol{\xi}|}H_1^{(1)}(\kappa|\boldsymbol{x}-\boldsymbol{\xi}|)+\frac{\mathrm{i}\kappa^2(x_1-\xi_1)^2}{4|\boldsymbol{x}-\boldsymbol{\xi}|^2}H_2^{(1)}(\kappa|\boldsymbol{x}-\boldsymbol{\xi}|),$$

$$\frac{\partial^2 G_{\mathrm{H}}}{\partial \xi_2 \partial x_2}(\boldsymbol{x},\boldsymbol{\xi}) = -\frac{\mathrm{i}\kappa}{4|\boldsymbol{x}-\boldsymbol{\xi}|}H_1^{(1)}(\kappa|\boldsymbol{x}-\boldsymbol{\xi}|)+\frac{\mathrm{i}\kappa^2(x_2-\xi_2)^2}{4|\boldsymbol{x}-\boldsymbol{\xi}|^2}H_2^{(1)}(\kappa|\boldsymbol{x}-\boldsymbol{\xi}|),$$

$$\frac{\partial^2 G_{\mathrm{H}}}{\partial \xi_1 \partial x_2}(\boldsymbol{x},\boldsymbol{\xi}) = \frac{\partial^2 G_{\mathrm{H}}}{\partial \xi_2 \partial x_1}(\boldsymbol{x},\boldsymbol{\xi}) = \frac{\mathrm{i}\kappa^2(x_1-\xi_1)(x_2-\xi_2)}{4|\boldsymbol{x}-\boldsymbol{\xi}|^2}H_2^{(1)}(\kappa|\boldsymbol{x}-\boldsymbol{\xi}|).$$

**Fourth Approach.**

$$\frac{\partial G_{\mathrm{H}}}{\partial x_j}(\boldsymbol{x},\boldsymbol{\xi}) = -\frac{\mathrm{i}\kappa(x_j-\xi_j)}{4|\boldsymbol{x}-\boldsymbol{\xi}|}H_1^{(1)}(\kappa|\boldsymbol{x}-\boldsymbol{\xi}|), \quad j=1,2.$$

**Example 1.** In Example 1 we used the following identities for the derivatives of the Bessel functions of the first kind and order $\mathsf{n}$, $J_{\mathsf{n}}(z)$, and the modified Bessel functions of the second kind and order $\mathsf{n}$, $K_{\mathsf{n}}(z)$, [1]:

$$\frac{d}{dz} J_{\mathsf{n}}(z) = \frac{\mathsf{n} J_{\mathsf{n}}(z)}{z} - J_{\mathsf{n}+1}(z), \quad \frac{d}{dz} K_{\mathsf{n}}(z) = \frac{\mathsf{n} K_{\mathsf{n}}(z)}{z} - K_{\mathsf{n}+1}(z).$$

For the evaluation of the functions $J_{\mathsf{n}}(z)$ and $K_{\mathsf{n}}(z)$ we used the MATLAB® commands `besselj(n,`$z$`)` and `besselk(n,`$z$`)`, respectively.

Department of Mathematics and Statistics, University of Cyprus/ Πανεπιστημιο Κυπρου, P.O.Box 20537, 1678 Nicosia/Λευκωσια, Cyprus/Κυπρος
*E-mail address*: andreask@ucy.ac.cy

Department of Applied Mathematics, University of Leeds, Leeds LS2 9JT, UK
*E-mail address*: amt5ld@maths.leeds.ac.uk